



# Chapter 6

## Diffraction limited single virion tracking in SPIM

*You do the light-sheet, we do the heavy-sheet*

— Romane Lane

Herpesviruses are among the most complex and largest of the clinically relevant viruses and establish life-long infections in their hosts. They are widespread in vertebrates and humans, with up to 85 % of the population worldwide being infected by Herpes Simplex Virus (HSV)-1 and around 25% by HSV-2. HSV-1 is the most extensively studied herpesvirus, and is a general model for other alphaherpesviruses. Infections by the nine known human herpesviruses are associated with many serious diseases including certain lymphomas and life-threatening conditions in immune-compromised patients [[1]]. Viral infections begin when infectious virus particles (virions) invade the organism by attaching to, and entering, susceptible cells. The virus hijacks the cellular machinery to replicate and produce progeny virus particles which then spread further infection. Herpesviruses pass through two distinct stages in their life cycle: lytic replication and latency. Among the key steps within the lifecycle and remains about the later stages of the infection cycle, the assembly of virus particles and their egress from the cell. Assembly and egress of viruses are essential stages in the herpesvirus lytic replication and contribute directly to pathogenesis. Imaging these processes, in particular, is an important goal of biomedical research.

### 6.0.1 Herpesvirus structure

In herpesviruses, the DNA genome is packaged in a nucleocapsid which is enveloped by a lipid membrane containing many viral membrane proteins. Nucleocapsid and envelope are separated by a complex, proteinaceous matrix called the tegument. The capsid is built up by the capsomers (capsid proteins) and possesses an icosahedral symmetry [4]. The tegument is a densely packed protein layer around the nucleocapsid, and essential for structural integrity and functionality of the virion. While the nucleocapsid structure and protein composition is well understood, much less is known about the structure and assembly of the tegument. The tegument can be divided into inner tegument (capsid-associated part) and outer tegument (envelope-proximal part). For HSV-1, more than 20 viral tegument proteins are known [5, 6] and listed in Table 6.1. Most of these tegument proteins possess multiple functions aiding in the entry of viruses into the cell; transport of incoming nucleocapsids to the nuclear pore and genome release; as well as nuclear assembly and egress; nucleocapsid maturation and directed release from the cell. Contained in the viral envelope of HSV-1 are at least 11 glycoproteins as well as several membrane-associated proteins which play important roles in viral entry and egress as well as virus-induced cell fusion [2, 7].

The proteins considered in this work are VP26, VP1/2 and VP16. VP26[1] and VP1/2 are structural proteins found in the capsid. VP16 is a tegument protein which complexes with host DNA to induce gene transcription, the initiation of gene expression.

### 6.0.2 Herpesvirus infection cycle

To initiate infection, herpesviruses first bind to cellular surface proteins which act as virus receptors as in Fig. 6.1. Then, by direct fusion to the plasma membrane or by endocytosis [8], the viral capsid is delivered into the cytosol. Incoming capsids are actively transported towards the nuclear pore complexes by exploiting microtubules within the cell [9, 10]. The capsid then releases the viral DNA through the nuclear pores into the nucleus [11]. Virion proteins drive the initial transcription to produce mRNAs. Translation of these early mRNAs promotes further phases of viral gene transcription and replication of the viral DNA. Replication of the viral DNA is achieved through actions of viral polymerases and other viral replicative machinery. These replicated DNAs are used as templates for mRNAs, which produce viral

**Table 6.1** HSV-1 virion components with alternative names in brackets. gXX refers to glycoproteins; VPXX refers to viral proteins; PK refers to protein kinase; ( $\alpha$ -TIF) refers to alpha transinducing factor; and (?) means the protein is suggested but not confirmed. Table from Mettenleiter [2].

Capsid	Tegument	Envelope
UL18 (VP23)	UL4 (?)	UL1 (gL)
UL19 (VP5)	UL11	UL10 (gM)
UL35 (VP26)	UL13 (PK; VP18.8)	UL20 (?)
UL38 (VP19c)	UL14	UL22 (gH)
	UL21	UL27 (gB)
UL6	UL36 (VP1/2)	UL43 (?)
UL25	UL37	UL44 (gC)
	UL41	UL45
	UL46 (VP11/12)	UL49.5 (gN)
	UL47 (VP13/14)	UL53 (gK)
	UL48 (VP16, $\alpha$ -TIF)	US4 (gG)
	UL49 (VP22)	US5 (gJ) (?)
	UL51	US6 (gD)
	UL56 (?)	US7 (gI)
	ICP0	US8 (gE)
	ICP4	US9
	US3 (PK)	
	US10	
	US11	

structural proteins, and are also packaged into capsids [[4]]. The egress pathway follows four steps (Fig. 6.1):

1. Capsid assembly and genome encapsidation in the nucleus,
2. Primary envelopment and de-envelopment at the nuclear envelope,
3. Tegumentation and secondary envelopment in the cytoplasm,
4. Exocytosis at the plasma membrane or cell-to-cells spread at cell junctions.

In the nucleus, the capsid proteins coassemble autocatalytically with and around the *portal complex* in late infection [[4]]. After capsids are formed and packaged in the nucleus, the capsids traverse the nuclear envelope. The nuclear envelope consists of a double membrane, the Inner Nuclear Membranes (INM) and Outer Nuclear Membranes (ONM). The capsids bud into the INM (primary envelopment) to form an enveloped particle in the perinuclear space, fuse with the outer nuclear membrane (de-envelopment) and are released into the cytoplasm [[12]]. In the cytosol, the capsids associate with more tegument proteins and bind onto and bud into cytoplasmic membranes derived from endosomes and/or the trans-Golgi network (secondary envelopment) [[13, 14]]. Although details of the mechanisms are not well understood, tegument maturation is likely directly connected to secondary envelopment via direct protein-protein interactions. Enveloped virions are finally secreted from cells by exocytosis [[15, 16]].

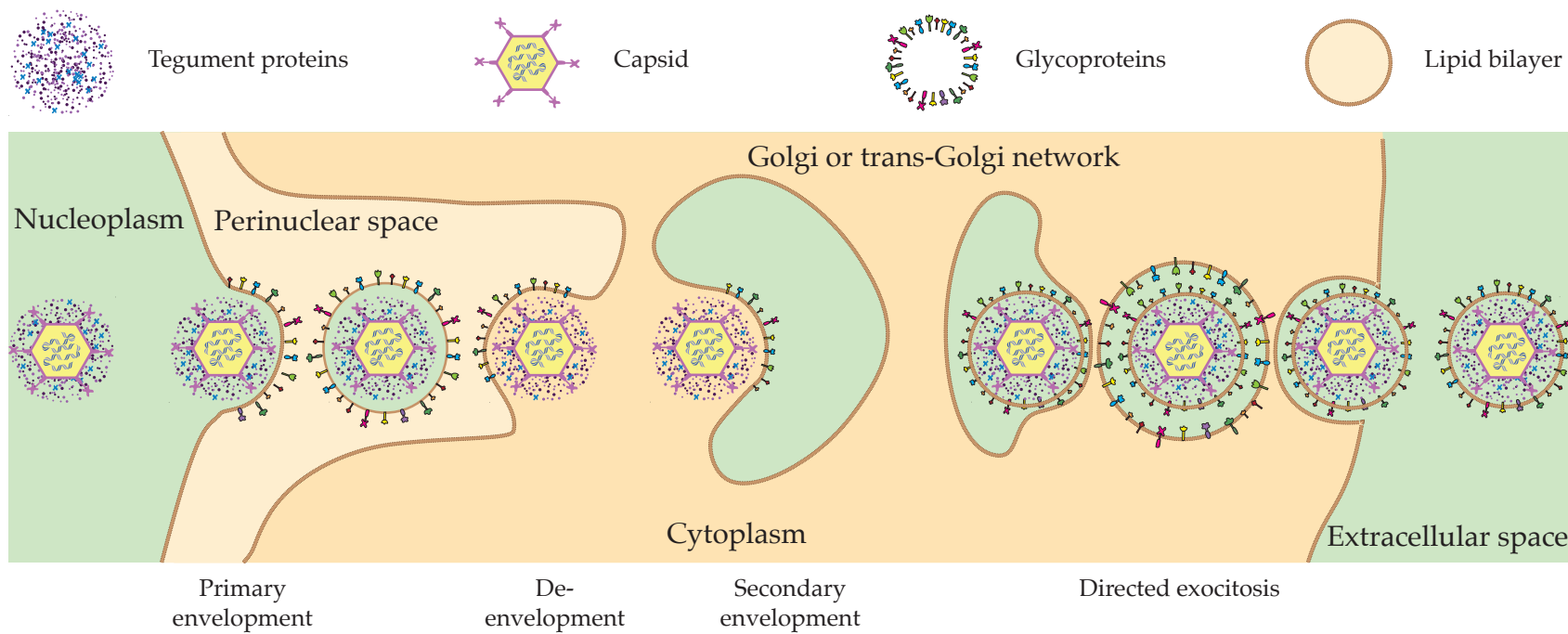


**Fig. 6.1** Scheme of assembly and egress pathway of virus particles. After capsids are formed in the nucleus, they bud into the INM (primary envelopment) to form an enveloped particle in the perinuclear space. These particles fuse with the ONM (de-envelopment) and are released into the cytoplasm, leaving the envelope in the ONM. In the cytosol, capsids bind onto and bud into cytoplasmic membranes (secondary envelopment), and enveloped virions are secreted from cells (release). Figure inspired by [[2]].

## 6.1 Single particle tracking microscopy

While optical imaging is generally limited to a lateral resolution of  $\sim 250\text{ nm}$  by diffraction, sparse emitters can be localised with much higher precision by mathematical image analysis methods; such as fitting a parametric equation to their image data. Tracking individual particles is an important tool for modern biology. It has been used to study intracellular transport of mRNA [Spille2015a] and by observing cell membrane dynamics [Cognet2014]. Many studies exist on intercellular and intracellular viral trafficking using single particle tracking [(reviewed in [43])]. Only a few and recent works exclusively probe the molecular egress pathway of herpesviruses. Hogue *et al.* [[16]] used Total Internal Reflection Fluorescence (TIRF) microscopy to selectively visualise fluorescent Pseudorabies viruses near the plasma membrane and follow them during exocytosis. Sandbaumhüter *et al.* showed, by a motility analysis of fluorescent HSV-1, that directed transport of cytosolic capsids was dependent on both tegument proteins pUL36 and pUL37 [[44]]. Virus trafficking and how viruses penetrate the nucleus of a cell have also been studied using Single Particle Tracking (SPT) [Brandenburg2007]. Due to a limited depth of field, particles tracked in a Three Dimensional (3D) volume tend leave the axial detection range. Several technical approaches already exist to perform SPT in three dimensions [[46-49]].

In orbital tracking microscopy [3], a laterally rotating spot orbits a target particle, any decline in the signal as measured at an angle then corresponds to a correction of the centre of the orbit. By splitting the image across two planes a further axial correction can be made by adjusting the detecting objective lens position such that the orbiting intensity is equal in both plane image planes. This technique was applied to track Prototype Foamy Virus (PFV) in real-time inside cells.

In this work HSV-1 virions will be observed using light-sheet microscopy. The light-sheet microscope will use an astigmatic lens in the detection path to modify the detection Point Spread Function (PSF) so that it may track single particles laterally and axially.

### 6.1.1 Particle detection

Particle tracking can be broadly described as a two stage process, spatial detection then temporal tracking. Crocker *et al.* define a particle tracking method as consisting of the following computable steps. Each image is first corrected for any distortion or error from the digitation process, followed by bandpass filtering to suppress image

noise. Second, local pixel value maxima (or minima depending on the nature of the particle problem) pixels with local maximum brightness are identified as *candidate* particles. A centroid (centre of mass) fitting procedure is employed to infer particle location under the assumption that, point-like particles with symmetric images are being observed. By fitting a Gaussian profile, or even the particle image's centre of mass in simple cases, particle position can be estimated with sub-pixel accuracy. Typically, iterative least squares fitting is used due to its ease of implementation, speed, precision and robustness.

### 6.1.2 Particle tracking or linking

Approaches to the linking of detected particles include simple nearest-neighbour[4] which assigns lineage to the nearest detected particle in the following frame, making it susceptible to misassignment in the case of occlusions. Multi-frame associations use the the additional available frames to increase the confidence in an assignment, these techniques include multiple hypothesis tracking[5], dynamic programming [6] and combinatorial schemes [7], with or without explicit use of motion models and state estimation (such as Kalman filtering [8]).

### 6.1.3 Light sheet single particle tracking

Spille *et. al.* proposed using light-sheet microscopy for tracking single particles over long periods. An essential aspect of the method was to shift their light-sheet and detection objective at each recorded frame so that the particle was repositioned to the centre of the sheet and did not drift outside of the illumination volume. Alternatively, the entire sample could be moved relative to a static sheet. Spille demonstrated this technique very successfully on a single molecule of mRNA (diameter 50 nm [Spille2015a]) moving on the membrane of a nucleus(see Fig. 6.4). Particle tracking results within the image data stack were then combined with information about the movement of the imaging volume to return estimates of particle movement within the specimen.

## 6.2 Astigmatic tracking

To successfully reposition the light-sheet for axial particle tracking precise axial localisation (within the illumination sheet) is needed. Spille *et. al.* installed a weakly

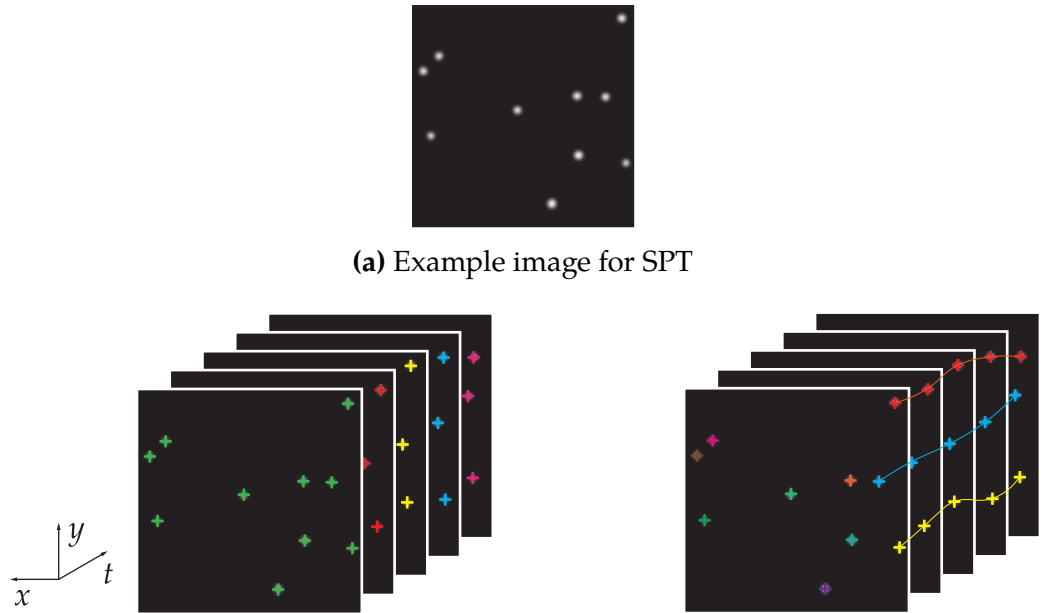
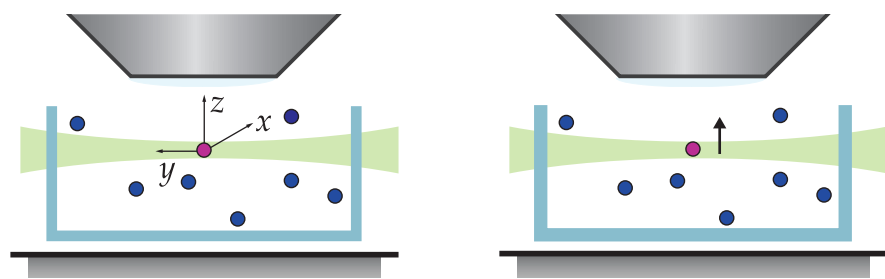


**Fig. 6.2** Routine for detecting and tracking particles.

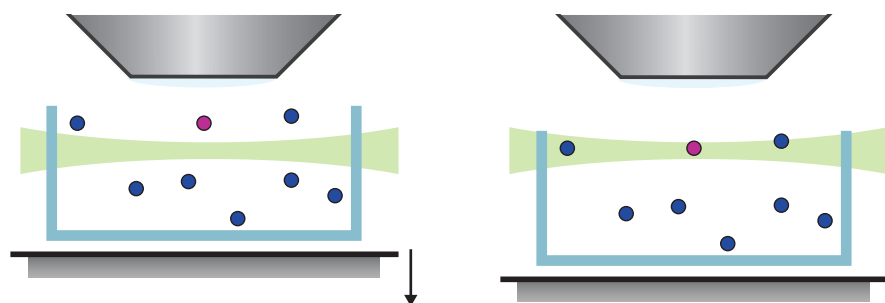
$$\begin{pmatrix} x_0 & y_0 & t_0 \\ x_1 & y_1 & t_0 \\ \dots & \dots & \dots \\ x_0 & y_0 & t_1 \\ x_1 & y_1 & t_1 \\ \dots & \dots & \dots \\ x & y & t \end{pmatrix} \quad (6.1)$$

$$\begin{pmatrix} x & y & t_0 & n_0 \\ x & y & t_1 & n_0 \\ \dots & \dots & \dots & \dots \\ x & y & t_0 & n_1 \\ x & y & t_1 & n_1 \\ \dots & \dots & \dots & \dots \\ x & y & t & n \end{pmatrix} \quad (6.2)$$



**(a)** Sample particles in chamber mounted on a fast axial translator. **(b)** The particle moves out of the light-sheet e.g. due to diffusion or flow

A static particle is localised in  $xy$



**(c)** The  $z$  stage repositions so that particle is within light-sheet **(d)** Particle is now back in light-sheet and  $z$  position is recorded

**Fig. 6.4** Routine to track particles three dimensionally using light-sheet imaging.

cylindrical lens within the detection optics adding astigmatism to the point spread function of the microscope. The asymmetry in focal lengths in the imaging plane axes results in an overall axial asymmetry in the detection PSF, for point sources this allows axial position to be encoded in the recorded image. This technique was used to great effect in *direct* stochastic optical reconstruction microscopy (dSTORM) and PALM systems, which rely on the localisation of point emitters to create 3D super-resolution volumes [9]. The range over which a cylindrical lens can axially encode is, at most,  $\sim 1 \mu\text{m}$  before the non-linearity in the astigmatism becomes too great and the PSF is too blurred to fit computationally.

### 6.2.1 Axial localisation

In a typical 3D localisation workflow, the position of the emitter is first localised laterally in Two Dimensional (2D), and then axially. Assuming an accurate localisation in 2D, the image of the point emitter is then localised axially. With each of the methods presented here, The following methods can be used for axial calibration, each requires a monotonic calibration measurement with a known volume of the sample space.

#### Gaussian fitting

The ratio of the Full-Width at Half-Maximum (FWHM) of the Gaussian along the major and minor axes will produce a calibration curve for axial position. The major and minor axis widths are obtained by fitting a 2D Gaussian function to the rotated and centered point image. However, this technique is computationally expensive and recovering axially position by fitting a 2D Gaussian is too slow for real time localisation and tracking. As such this technique is only useful in post-capture analysis of images already recorded.

#### Template matching

The cross correlation of two signals returns a single value representing an unnormalised similarity of the two signals. Cross-correlation requires no fitting step and scales in computational complexity with the image as  $O(n^2)$ . As such using fewer pixels to recover axial position allows this technique to function in real-time. Provided the astigmatism calibration images vary smoothly with axial position , a cross-correlation for every image in the calibrated stack may not be needed. By using

all the images in the calibration stack, the computational time increases in proportion to the number of axial images in that stack. The ratio of the cross correlation of with a pair of calibration images spaced axially and equally about the focal centre of the stack will however give an estimate of particle position. This estimate is sufficient for real-time tracking; and provided the images of the point-emitter are recorded, a more accurate axial localisation step can be applied in post-capture analysis. The discrete cross-correlation function is defined as follows:

$$(f \star g)[n] \stackrel{\text{def}}{=} \sum_{m=-\infty}^{\infty} f^*[m] g[m+n] \quad (6.3)$$

Where  $f^*$  is the complex conjugate. Similarly the covariance of the calibration of an image or volume can be used lowering the computational complexity again.

### 6.2.2 Simulations of image data to test particle tracking methods

To verify that single particle tracking in light-sheet microscopy was possible, the diffusion of a single diffraction limited particle was simulated *in silico* (see Fig. 6.5). To create the simulation, the particle was modelled to take a random walk with discrete time steps  $dt = \sim 0.1$  ms across a single imaging exposure of 40 ms. This simulated how the particle would appear to move within the light-sheet during each frame acquisition, creating *dynamic blur* as described by Savin and Doyle[10]. The intensity of the final image of a particle was attenuated as its position varied within the Gaussian light-sheet to the Gaussian illumination intensity of the light-sheet axially ( $z$ ) and laterally ( $x, y$ ) as per:

$$w_0 = 1.4\lambda \frac{\text{NA}}{n} \quad (6.4)$$

$$w(y) = w_0 \sqrt{1 + \left(\frac{y}{y_R}\right)^2} \quad (6.5)$$

$$y_R = \frac{\pi w_0^2}{\lambda} \quad (6.6)$$

$$I(x, y, z) = I_0 \left( \frac{w_0}{w(y)} \right)^2 e^{-2 \frac{z^2}{w(y)^2}} \quad (6.7)$$

Where  $w_0$  is the beam waist; NA is the numerical aperture of the excitation objective,  $n$  is the refractive index of glass;  $\lambda$  is the wavelength of excitation light;  $y_R$  is the Rayleigh length and  $w(y)$  is the beam waist through  $y$ .

### 6.3 Motion-induced astigmatic axial localisation error

It was demonstrated in the computational simulations and by Savin and Doyle [10], that a particle moving in a real system will demonstrate a motion blur. In an astigmatic imaging system, the image of a particle does not vary linearly with the distance the particle has travelled axially during the image exposure period. A single particle moving quickly in the  $xy$  plane will appear to stretch and the localised position of the particle will be the average of the start and end position. In order to study axial localisation using motion-blurred image data acquired with an astigmatic system, the following image formation approximation was developed.

A Gaussian was convolved with the single point in space, with the assumption that the depth of field of the detection objective was the same as the width of the light-sheet ( $D_{\text{objective}} = 2w_0$ ) and that intensity across the sheet was uniform. A Gaussian function being used to model a static particle is a valid assumption as Gaussian models are used in the fitting process for localisation from the pixel data.

To simulate a particle being imaged using an astigmatic lens the standard Gaussian equation of:

$$f(x, y) = e^{-\frac{x^2+y^2}{2\sigma^2}} \quad (6.8)$$

was modified to use a simple model of astigmatism by assuming that  $\sigma$  depends on  $z$  such that:

$$\sigma \rightarrow \sigma(z) = |kz + c| \quad (6.9)$$

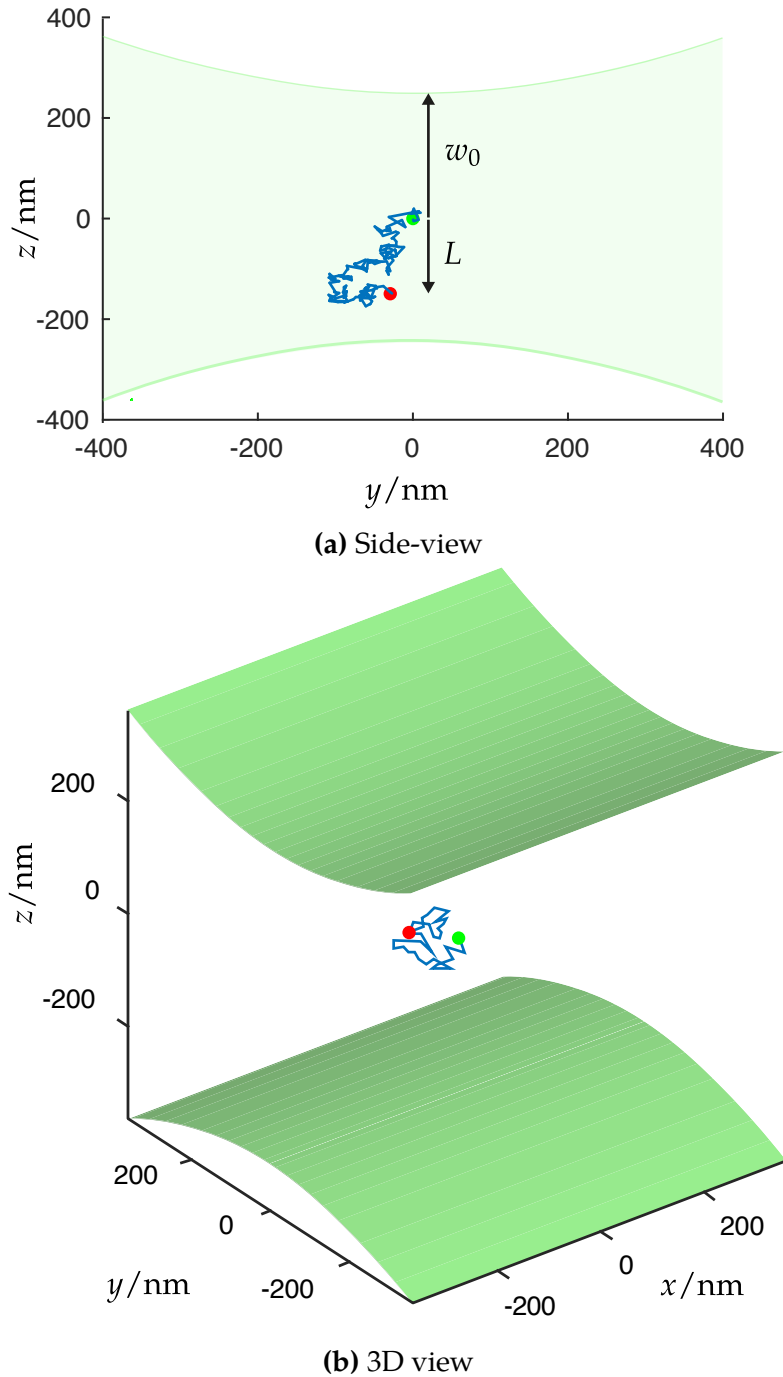


**Fig. 6.5** Simulations of a single particle diffusing within a light-sheet with a viscosity in a Newtonian fluid medium with a viscosity of 1.31 mPa s (25 % glycerol in water [11]) at a temperature of 25 K. The particle track length (blue, from green to red) corresponds to 40 ms of real time

Where  $k$  is how quickly the Gaussian narrows, which is an analogue of using a more astigmatic imaging system.  $c$  describes the radius of the PSF when there is no astigmatism, which is when the particle is in focus at  $z = 0$ . It is useful to express  $k$  in terms  $a$ , where  $a$  is a function of  $c$  and  $w_0$  such that the Gaussian is  $\frac{1}{a}$  narrower when at the extrema of the depth of field,  $z = w_0$ .

$$\implies k = \frac{ac}{w_0} \quad (6.10)$$

To scale the model to three dimensions, we assume  $k = -k$  in the  $y$  axis, forcing the astigmatic model of the PSF to narrow in  $y$  as  $x$  broadens, and visa versa.

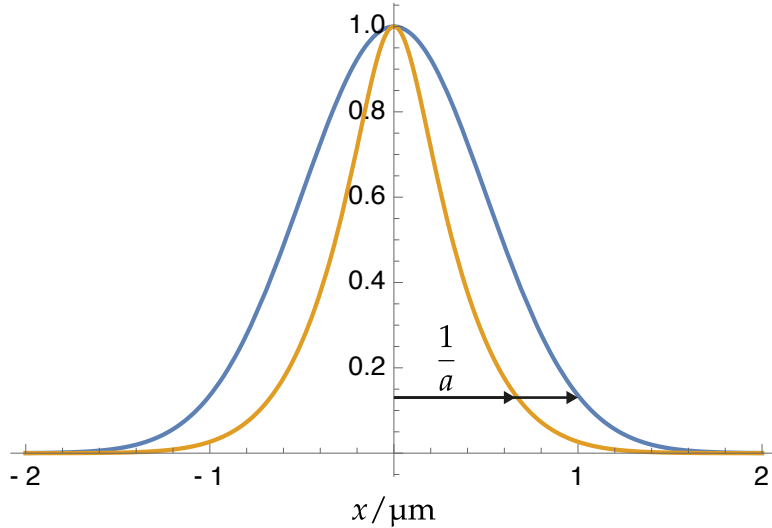
$$f(x, y, z) = e^{-\frac{x^2}{2(|kz+c|)^2} + \frac{y^2}{2(|-kz+c|)^2}} \quad (6.11)$$

To make calculations tractable, all modelling was considered in  $xz$  as the effect of astigmatism in  $y$  is independent. The approximate PSF is defined such that no motion blur is considered:

$$\text{PSF}_{\text{Approximate}} = e^{-\frac{x^2}{2\sigma(z)^2}} \quad (6.12)$$

Assuming that the particle moves in the  $z$  direction, with uniform speed and uniform emission of photons en-route, integrating the approximate PSF gives the numerical PSF as subject to dynamic blur:

$$\text{PSF}_{\text{Numerical}} = \frac{1}{L} \int_0^L e^{-\frac{x^2}{2\sigma(z)^2}} dz \quad (6.13)$$



(a) Normalised peak intensity

**Fig. 6.6** (a) Approximate versus numerical PSF profile of a particle using normalised peak intensity, a weaker model for astigmatism (b) Uses normalised area of the approximate and numerical PSFs for a more accurate model of astigmatism

The integral has to be scaled by  $\frac{1}{L}$  to rescale the peak value to unity. The resultant function is then comparable with  $\text{PSF}_{\text{Approximate}}$  as shown in Fig. 6.6a. Evaluating (6.13) gives:

$$\text{PSF}_{\text{Numerical}} = \frac{2c(aL + w_0)e^{-\frac{w_0^2 x^2}{2c^2(aL+w_0)^2}}}{2acL} \quad (6.14)$$

$$+ \frac{w_0 x \sqrt{2\pi} \text{Erf}\left(\frac{(w_0 x)}{\sqrt{2}(acL+cw_0)}\right)}{2acL} \quad (6.15)$$

$$+ \frac{w_0 \left(2ce^{-\frac{x^2}{2c^2}} + \sqrt{2\pi}x \text{Erf}\left(\frac{x}{\sqrt{2}c}\right)\right)}{2acL} \quad (6.16)$$

### 6.3.1 Area analysis

For Gaussian-like functions the total area under the curve is proportional to  $\sigma(z)$ , so by comparing the area covered by the approximate and numerical PSFs, a valid measure of error may be obtained. This analysis does not work for normalised

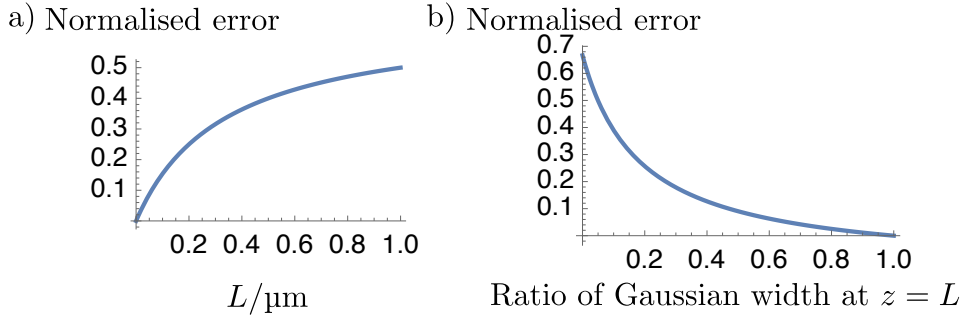


**Fig. 6.7** (a) The absolute error from Equation 6.20 was plotted against distance the particle travels in a single exposure frame. (b) The degree of astigmatism  $k$  was reframed such that it a substitute parameter represented the ratio of the width of the Gaussian at  $z = 0$  and  $z = L$ . This graph shows that as the ratio approaches unity the error due to astigmatic smearing becomes zero. However, when the ratio of the widths approaches zero, the error does not approach infinity as would be expected.

Gaussians functions as the area is unity in each case. To retrieve the areas of each modelled PSF, they were integrated across all space:

$$\int_{-\infty}^{\infty} \text{PSF}(x, \dots)_{\text{Approximate}} dx = \frac{\sqrt{2\pi}}{\sqrt{\frac{1}{\left(\frac{acL}{w_0} + c\right)^2}}} \quad (6.17)$$

$$\int_{-\infty}^{\infty} \text{PSF}(x, \dots)_{\text{Numerical}} dx = \sqrt{\frac{\pi}{2}} \left( \frac{2(aL + w_0)}{aL \sqrt{\frac{w_0^2}{c^2(aL+w_0)^2}}} - \frac{2w_0}{a \sqrt{\frac{1}{c^2}L}} + c \left( -\frac{aL}{w_0} - 2 \right) \right) \quad (6.18)$$

The absolute error between these two functions is computed by:

$$\frac{\int_{-\infty}^{\infty} \text{PSF}(x, \dots)_{\text{Approximate}} dx - \int_{-\infty}^{\infty} \text{PSF}(x, \dots)_{\text{Numerical}} dx}{2 \int_{-\infty}^{\infty} \text{PSF}(x, \dots)_{\text{Approximate}} dx + \int_{-\infty}^{\infty} \text{PSF}(x, \dots)_{\text{Numerical}} dx} \quad (6.19)$$

$$= 2 \frac{-\frac{2w_0}{aL \sqrt{\frac{w_0^2}{c^2(aL+w_0)^2}}} + \frac{2w_0}{a \sqrt{\frac{1}{c^2}L}} + c \left( \frac{aL}{w_0} + 2 \right)}{\frac{2(2aL+w_0)}{aL \sqrt{\frac{w_0^2}{c^2(aL+w_0)^2}}} - \frac{2w_0}{a \sqrt{\frac{1}{c^2}L}} + c \left( -\frac{aL}{w_0} - 2 \right)} \quad (6.20)$$

Equation (6.20) details how the absolute error between the approximate and numerical PSF varies as the particle's location changes by a displacement  $L$ , assuming uniform velocity, during the image exposure time as shown in Fig. 6.7. This length  $L$  may then be computed from the three dimensional diffusivity of a small particle from the diffusivity  $D$ :

$$D = \frac{kT}{6\pi\mu r} \quad (6.21)$$

Where  $k$  is Boltzmann's constant,  $T$  is temperature,  $\mu$  is the viscosity of the medium,  $r$  is the radius of the particle, from  $D$  the average distance of diffusion  $\langle w \rangle$  can be computed:

$$\langle w \rangle^2 = q_i D t \quad (6.22)$$

Where  $q_i$  is the dimensionality of the diffusion and  $t$  is the time elapsed. By setting the parameters to realistic world values:  $T = 298 \text{ K}$ ;  $\mu = 0.002 \text{ N s m}^{-1}$ ;  $k = 1.3806 \times 10^{-23} \text{ m kg}^2 \text{ s}^{-2} \text{ K}^{-1}$ ;  $c = r = 100 \text{ nm}$ ;  $a = \frac{1}{5}$ ;  $w_0 = 0.5 \mu\text{m}$ ; there is an average expected axial localisation error of  $\sim 25\%$  using Equation (6.20) which is caused by dynamic blur in astigmatic imaging systems.

## 6.4 Results

### 6.4.1 Cellular imaging

Virally infected HeLa cells were mounted on cover glass and imaged using the modified light-sheet microscope. The cells were infected with HSV-1 expressing tegument proteins fused to fluorescent proteins (VP26-mTurquoise, VP1/2-dTomato, VP16-cYFP). Trypsin was used to help lift cells in culture into solution and was left to act for 3 min. 10% Foetal Bovine Serum (FBS) was added to deactivate the Trypsin as it is a protease enzyme and will further degrade the cells. Coverslips were submerged in the cellular solution and left to adhere and culture on the glass. 3% paraformaldehyde was used to fix cells for the preliminary visualisation experiments. The glass coverslips were mounted in the custom imaging chamber discussed in Chapter ?? for light-sheet imaging.

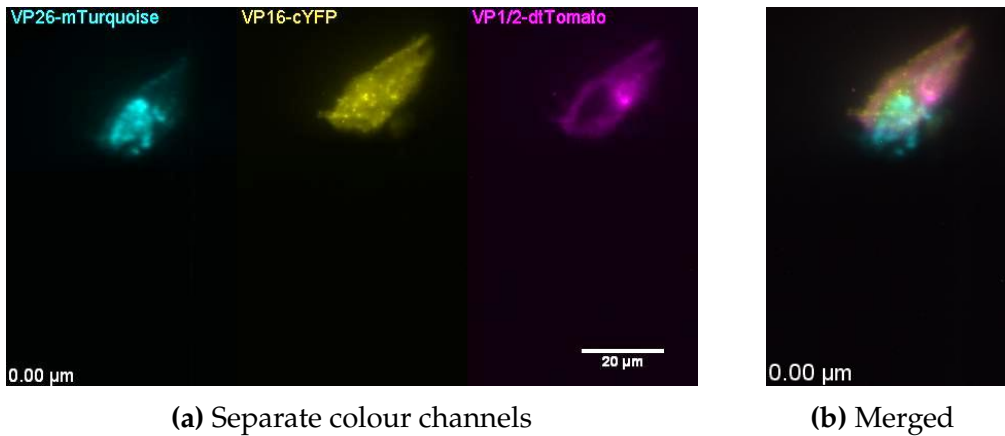


**Fig. 6.8** HSV-1 viral proteins volumetrically imaged in fixed cells using the light-sheet fluorescence microscope. VP26 is a capsid protein and marks where the viral capsid is in the nucleus. VP1/2 is a capsid protein that is recruited by the capsid and transcribed by the cell. VP16 is a tegument protein that is recruited to the viral tegument and also transcribed by the cell.

## 6.5 Observations and tracking of virions using light-sheet microscopy

The secondary optical relay was set to  $2.5 \times$  magnification, giving  $62.5 \times$  at the sample plane, to ensure the image resolution was not Nyquist limited. This ensured the pixel width was sufficiently less than the size of the PSF width, so that the PSF width could be accurately estimated. The weakly cylindrical lens ( $f = 1\text{ m}$ ) was inserted in between the secondary relay and the camera unit at 40 mm away from the aperture of the camera. The cylindrical lens was inserted in between the camera and the tube lens as adding the cylindrical lens in an infinity space would have amplified the astigmatic effect (to beyond usable), and disabled any tuning of the astigmatism through positioning.

For calibration of the axial particle tracking, an agarose gel of beads containing 200 nm fluorescent beads, was imaged with the objective lens and the light-sheet synchronously swept through small axial steps. Moving the stage would have better emulated how a particle would appear, however, the mechanical resolution and hysteresis of the translation stage made this infeasible.

To compare the quality of the calibration, the curves were fit with straight lines and their with the respective regression statistics present in Table 6.2. It was shown that using cross-correlation, provides larger  $R^2$  value and hence a better fit for a

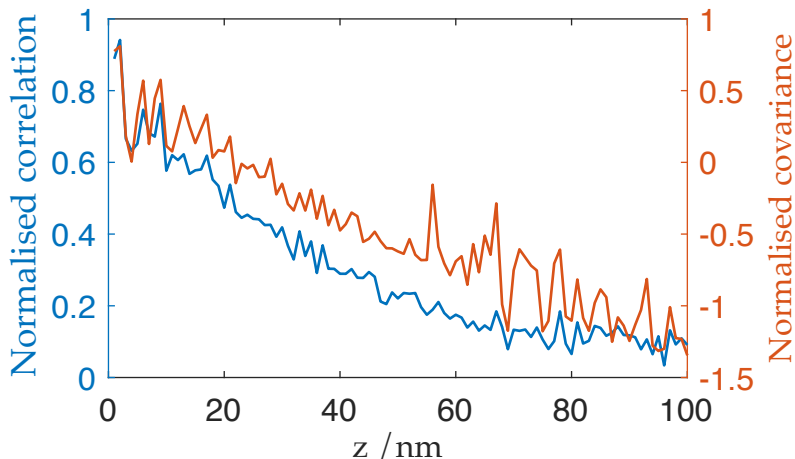


**Fig. 6.9** Curves showing calibration between axial depth within the light-sheet and template matched cross-correlation (blue) and covariance (orange). Normalisation here refers to the input images being normalised, which in the case of covariance does not necessarily ensure a normalised output.

linear model. However there is a lower residual sum of squares, meaning co-variance may reduce the error in fitting.

**Table 6.2** Table of the regressional analysis for the calibration curves in Fig. 6.9. RSS: Residual sum of squares;  $R^2$ : Coefficient of determination; RMSE: Root mean square error

Metric	RSS	$R^2$	RMSE
Covariance	0.633	0.8569	0.12037
Cross-correlation	2.984	0.8904	0.08037

## 6.6 Conclusions

It was shown that the inverted light-sheet system described in this work, is capable of axially localising particles. This was demonstrated experimentally using static sub-diffraction limit particles with a view to applying the same techniques to dynamic particles. It was also shown that dynamic particles within when tracked astigmatically are susceptible to a localisation error on the order of 25 % given standard imaging and biological conditions. This was demonstrated on a model system numerically.

The detection objective used in the light-sheet system was affected by significant spherical aberration. The spherical aberration was addressed using a bespoke tool to

manually rotate the correction collar on the objective lens; this then lead to dramatic coma effects which had otherwise been masked by spherical aberration. The latter aberration could not be corrected for which made Gaussian fitting infeasible for axial localisation. However, template matching techniques did still produce a viable calibration curve that could be used, with cross-correlation being the lowest mean square error and the more reliable estimator.

## 6.7 Future work

It was also shown that a Nyquist limited cellular image could also be acquired using this system. By using a CO<sub>2</sub> free buffer, such as HEPES, HeLa could be imaged in this system for long enough to observe viral egress within a live cell. The next step for particle tracking would be to observe single particles diffusing in a viscous medium that acts as an analogue for the cell. Once both of these have been demonstrated, SPT of viral egress from a live cell may be achieved.

### 6.7.1 Neural networks

In this work, the techniques presented for localising particles, in an astigmatic system, rely on a singular calibrated point emitter, the template. A population of point-emitters with known axial positions would help mitigate potential axial localisation errors. It is possible to align multiple calibration volumes and create an averaged or model calibration volume to work with, though this method relies heavily on the sub-pixel alignment step to reduce error.

Training a NN could be a more robust approach. NNs take multiple inputs and produce a single output based on a back propagation step which helps determine the weightings on the *neurons* in the hidden layer or layers. Convolutional neural networks work in a similar fashion except that the weightings are image convolution steps; by using convolution steps the overall size of the neural network needed reduces making image recognition possible. By training a neural network on a given input segmented input image, with the known output of axial position, a fast and accurate machine for producing axial localisations could be utilised. NNs are also computationally inexpensive as most of the effort put in occurs during the training step.

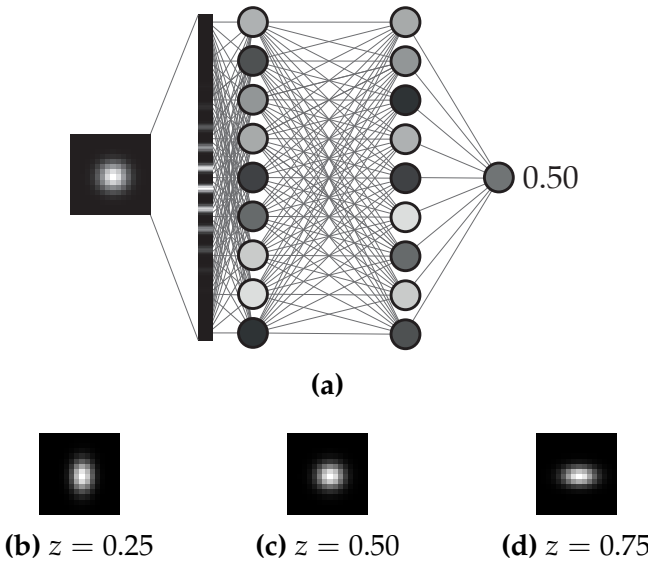


**Fig. 6.10** (a) A schematic of a trained Neural Network (NN) converting a simulated image into an axial position. The image is first flattened and fed into a hidden layer of 10 neurons; the weighted outputs of these neurons are fed into the next layer; then those outputs are weighted and fed into a final output node with the range 0 to 1. (b), (c) and (d) are example simulated images showing astigmatism at their respective normalised axial position  $z$ .

Using a NN to predict the axial location of a bead from its image was briefly explored for feasibility. Simulated data was used from the model presented in Equation (6.11). The ground truth axial positions, as simulated, were then fed to the neural network which had a single output. 3000 example images were given to help the network converge more quickly, though this may be unrealistic in a real microscope. Fig. 6.11 shows that the absolute error of the NN, when compared to the ground truth, produces a normal distribution centered on 0.8 % with a variance of 3.7 %.

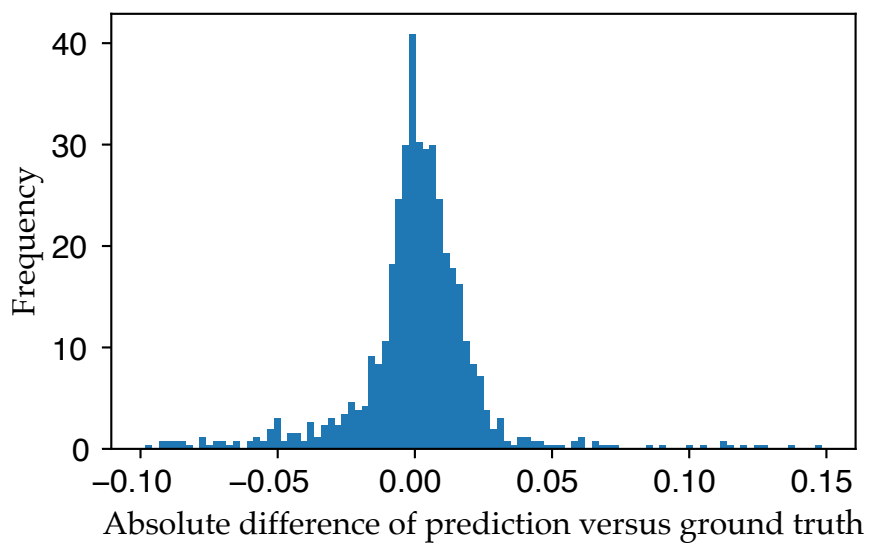


**Fig. 6.11** Histogram of a neural network predicting the axial positing of simulated astigmatic images. Assuming a normal distribution, the centre of the distribution is  $\mu = -0.008$  with a variance of  $\sigma = 0.037$ .

# References

1. Tang, X., Wu, J., Sivaraman, J. & Hew, C. L. Crystal Structures of Major Envelope Proteins VP26 and VP28 from White Spot Syndrome Virus Shed Light on Their Evolutionary Relationship. *Journal of Virology* **81**, 6709–6717 (2007).
2. Mettenleiter, T. C. Herpesvirus Assembly and Egress. *Journal of Virology* **76**, 1537–1547 (2002).
3. Dupont, A. & Lamb, D. C. Nanoscale Three-Dimensional Single Particle Tracking. *Nanoscale* **3**, 4532–4541 (2011).
4. Methods of Digital Video Microscopy for Colloidal Studies. *Journal of Colloid and Interface Science* **179**, 298–310 (1996).
5. Coraluppi, S. & Carthel, C. Recursive Track Fusion for Multi-Sensor Surveillance. *Information Fusion* **1**, 23–33 (2004).
6. Rink, J., Ghigo, E., Kalaidzidis, Y. & Zerial, M. Rab Conversion as a Mechanism of Progression from Early to Late Endosomes. *Cell* **122**, 735–749 (2005).
7. Sbalzarini, I. F. & Koumoutsakos, P. Feature Point Tracking and Trajectory Analysis for Video Imaging in Cell Biology. *Journal of Structural Biology* **151**, 182–195 (2005).
8. Ku, T.-C. *et al.* An Automated Tracking System to Measure the Dynamic Properties of Vesicles in Living Cells. *Microscopy Research and Technique* **70**, 119–134 (2007).

9. Huang, B., Wang, W., Bates, M. & Zhuang, X. Three-Dimensional Super-Resolution Imaging by Stochastic Optical Reconstruction Microscopy. *Science* **319**, 810–813 (2008).
10. Savin, T. & Doyle, P. S. Static and Dynamic Errors in Particle Tracking Microrheology. *Biophysical Journal* **88**, 623–638 (2005).
11. Segur, J. B. & Oberstar, H. E. Viscosity of Glycerol and Its Aqueous Solutions. *Industrial & Engineering Chemistry* **43**, 2117–2120 (1951).